Check for updates

ADVANCING EARTH AND SPACE SCIENCES

JGR Space Physics

RESEARCH ARTICLE
10.1029/2025JA034883

Special Collection:
Coupling Processes from Space to Earth

Key Points:

- Plasma sheet (PS) mass loading persists across all interplanetary magnetic field (IMF) orientations and solar wind speeds
- PS–E_Y increases monotonically with rising SW–E_{CY0} under southward IMF but shows a weak response under northward IMF
- Kinetic-E and ion temperature in the plasma sheet exhibit low correlation with SW–E_Y

Correspondence to:
H. Li,
hli@nssc.ac.cn

Citation:
Zhang, L., Dai, F., Li, H., Liu, A., Wei, X., Wang, C., et al. (2026). Dual-channel energy and mass coupling between the solar wind and magnetotail plasma sheet: Insights from machine learning-based partitioning. *Journal of Geophysical Research: Space Physics*, *131*, e2025JA034883. https://doi.org/10.1029/2025JA034883

Received 19 NOV 2025
Accepted 11 MAY 2026

Author Contributions:
Data curation: Andi Liu, Xuan Liu
Investigation: Jue Wang, Rui Zheng, Jing Yu
Methodology: Xinhua Wei, Jiye Wang, Wenchao Liu, Tieyan Wang
Project administration: Chi Wang
Software: Fanzhuo Dai
Writing – original draft: Lingqian Zhang
Writing – review & editing: Hui Li, James L. Burch, Wolfgang Baumjohann

© 2026. American Geophysical Union. All Rights Reserved.

Dual-Channel Energy and Mass Coupling Between the Solar Wind and Magnetotail Plasma Sheet: Insights From Machine Learning-Based Partitioning

Lingqian Zhang[1], Fanzhuo Dai[1], Hui Li[1], Andi Liu[2], Xinhua Wei[1], Chi Wang[1], Jiye Wang[3], Wenchao Liu[4], Jue Wang[4], Xuan Liu[3], Rui Zheng[3], Jing Yu[3], Tieyan Wang[5], James L. Burch[6], and Wolfgang Baumjohann[7]

[1]State Key Laboratory of Solar Activity and Space Weather, National Space Science Center, Chinese Academy of Sciences, Beijing, China, [2]College of Information and Communication Engineering, Beijing Information Science and Technology University, Beijing, China, [3]Information Engineering College, MinZu University of China, Beijing, China, [4]National Key Laboratory of Science and Technology on Space-Born Intelligent Information Processing, Beijing Institute of Technology, Beijing, China, [5]Department of Geophysics, School of Earth Sciences, Yunnan University, Kunming, China, [6]Southwest Research Institute San Antonio, San Antonio, TX, USA, [7]Space Research Institute, Austrian Academy of Sciences, Graz, Austria

Abstract Utilizing joint observations from the Magnetospheric Multiscale (MMS) and OMNI spanning from 2017 to 2021, we investigate the response of the Earth's plasma sheet (PS) to solar wind (SW) forcing. The PS is divided into three key regions in the downtail ($X < -10\ R_E$, Geocentric Solar Magnetospheric), that is, the current sheet (CS), central plasma sheet (CPS), and plasma sheet boundary layer, using a hybrid filter–decision tree model (HFDTM). The PSs of different regions were analyzed under four upstream SW speed and interplanetary magnetic field (IMF) conditions: low-speed northward (LSNW), low-speed southward (LSSW), high-speed northward (HSNW), and high-speed southward (HSSW). For each regime, we perform a comprehensive statistical analysis of key physical parameters, including the convective electric field (E_{CY}), kinetic electric field (E_K), and ion density (n_i) and temperature (T_i). Our main finding are as follows: (a) Ec_Y in the plasma sheet shows a monotonic increase with rising SW–E_{CY0} across all 3 PS regions under southward IMF, but ambiguous correlation with SW under northward IMF; (b) n_i shows a strong correlation with the solar wind under both IMF orientations, particularly during low-speed conditions; and (c) E_K and T_i consistently display weak correlations across all regimes, highlighting the dominant role of internal processes in plasma sheet evolution. These results support a dual-path coupling mechanism between the solar wind and the magnetosphere, characterized by persistent mass loading across all regimes, and an energy transfer pathway that is strong under the southward IMF but weak and primarily governed by internal energy relaxation processes under northward IMF.

Plain Language Summary The solar wind continuously interacts with Earth's magnetic environment, influencing space weather and geomagnetic activity. In this study, we use spacecraft observations and machine learning techniques to investigate how energy and mass from the solar wind enter and affect the magnetotail plasma sheet. We find that energy transfer strongly depends on the direction of the IMF, while mass loading persists under all solar wind conditions. In addition, some internal processes within the magnetotail, such as plasma heating, are largely independent of direct solar wind driving. These results improve our understanding of how solar wind energy and particles are processed in near-Earth space and contribute to better predictions of space weather dynamics.

1. Introduction

The solar wind continuously delivers energy and mass into the Earth's magnetosphere, driving a highly dynamic geospace environment that underlies space weather and geomagnetic activity (Axford & Hines, 1964; Dungey, 1961; Gonzalez et al., 1994; McPherron et al., 2015). At the core of this coupled system is the magnetotail plasma sheet, where solar wind energy is stored, transported, and ultimately dissipated into the inner magnetosphere and ionosphere, powering magnetospheric substorms and geomagnetic storms (Borovsky & Bonnell, 2001; Southwood, 2021; J. Y Wang et al., 2014). The solar wind–magnetosphere (S-M) interaction can be conceptualized as a dual-channel coupling process, comprising distinct yet interconnected pathways for energy transfer and mass transport. Energy coupling occurs primarily through large-scale magnetospheric current systems, where magnetic energy is cyclically loaded and unloaded via thinning and recovery of the cross-tail current sheet. This loading–unloading process is strongly modulated by the orientation of the interplanetary magnetic field, particularly its north–south (B_Z) component, which regulates dayside reconnection efficiency and the overall energy input into the magnetosphere (Baker et al., 1983; Borovsky et al., 1998; Myllys et al., 2015). In contrast, the mass content of the plasma sheet is derived from both direct solar wind entry and ionospheric outflows (Kistler et al., 2023), highlighting the fundamentally bifurcated nature of energy and mass pathways in the magnetosphere.

IMF B_Z plays a pivotal role in regulating the large-scale topology of the magnetosphere, determining whether the system evolves toward an open or closed magnetic configuration (Baker et al., 2007; Borovsky et al., 1997; Eastwood et al., 2015; Huang et al., 2003; Ma et al., 2020; McPherron, 1970; Zhang et al., 2019). Under southward IMF conditions (negative Bz), antiparallel magnetic field orientations between the solar wind and the dayside magnetosphere facilitate efficient magnetic reconnection at the subsolar magnetopause (Fuselier et al., 2011; Phan & Paschmann, 1996). This process permits magnetic flux and solar wind plasma to convect into the magnetotail lobes, resulting in enhanced Poynting flux transfer, mass loading of the plasma sheet, and increasing lobe magnetic pressure. The resulting compression of the plasma sheet intensifies the cross-tail current in the near-Earth region. The efficiency and timescale of this flux transport are governed by the solar wind convective electric field, defined as $E_{SW} = -V_{SW} \times B_{SW}$ (Gordeev et al., 2017; Kan & Lee, 1979; C. Wang et al., 2014). When strong and sustained southward IMF intervals occur (e.g., $E_{SW} > 0.5$ mV/m for more than 1 hr), the coupling between energy and mass becomes highly efficient, mediated by large-scale convection and current systems (Antonova & Ovchinnikov, 1999; Baumjohann et al., 1992; Zhang, Wang, Baumjohann, Rème, & Dunlop, 2015). Magnetic flux accumulation in the lobes leads to the formation of a thin cross-tail current sheet (CTCS) that stores increasing free energy. Once the CTCS reaches a critical threshold of instability, near-Earth magnetic reconnection is triggered, marking the onset of the unloading phase of substorm development (Baker et al., 1996; Baumjohann et al., 1999; Newell & Liou, 2011; Rostoker et al., 1988; Runov et al., 2021). Observational studies suggest that reconnection typically follows southward IMF turnings with an average delay of approximately 40 min, reflecting the time required for current sheet thinning and energy accumulation (Hill & Reiff, 1980; Samsonov et al., 2024; Zhang et al., 2016). Extended periods of southward IMF ($\geq$5 hr) can drive intense substorms and major geomagnetic storms, representing some of the most geoeffective solar wind driving conditions (Henderson, 2004; Lazzeri et al., 2024; Tulasi Ram et al., 2024). The strength and duration of the solar wind electric field are therefore critical parameters in modulating the magnetotail energy input and its subsequent dynamic reconfiguration.

In contrast, when the IMF B_Z turns northward (positive Bz), magnetic reconnection migrates from the subsolar point to high-latitude regions of the magnetopause, establishing a quasi-stable, unloading-dominated configuration within the magnetosphere (Guzdar et al., 2001; Kessel, 1996; Ogino et al., 1994; Song et al., 1999). This regime is characterized by reduced dayside reconnection efficiency and the suppression of substorm activity, reflecting a generally lower geoeffective of S-M coupling (Antonova & Ovchinnikov, 2001; Li et al., 2021; Petrukovich et al., 2003). The associated weakening of magnetic tension and cross-tail current systems results in diminished reconnection rates in the magnetotail, facilitating a transition toward a more quiescent magnetospheric state that emphasizes energy dissipation over accumulation (Guzdar et al., 2001). Although low-level reconnection in the tail may persist under these conditions, it primarily acts to dissipate residual magnetic energy rather than contribute to large-scale energy loading or substorm onset (Park et al., 2015; Peng et al., 2013; Zhang, Wang, Baumjohann, Rème, Dai, et al., 2015, 2016). Meanwhile, plasma sheet mass loading can continue through alternative non-E_{CY}-dependent mechanisms, including high-latitude lobe reconnection (Li et al., 2008), flank-side Kelvin–Helmholtz (K–H) instabilities (Fujimoto et al., 1998; Hasegawa et al., 2004; Miura, 1984; Terasawa et al., 1997), or viscous-like cusp injection driven by kinetic Alfvén waves (Johnson & Wing, 2009). These processes collectively contribute to the formation of the cold, dense plasma sheet (CDPS), a distinctive feature frequently observed during prolonged intervals of northward IMF (Fuselier et al., 2015; Li et al., 2005; Richard et al., 1994; Wang et al., 2007; Wing et al., 2005; Øieroset et al., 2005).

While the IMF B_Z component primarily regulates the transition between loading and unloading phases within the magnetospheric system, the IMF B_Y component plays a crucial structural role by shaping the global configuration of the magnetotail (Hu et al., 2009; Phan et al., 2013; Tenfjord et al., 2018). The penetration of IMF B_Y into the magnetosphere occurs over timescales ranging from tens of minutes to several hours, depending on the magnitude

21699402, 2026, 5, Downloaded from https://agupubs.onlinelibrary.wiley.com/doi/10.1029/2025JA034883 by Hui Li - Center For Space Science And Applied Research, CAS , Wiley Online Library on [21/05/2026]. See the Terms and Conditions (https://onlinelibrary.wiley.com/terms-and-conditions) on Wiley Online Library for rules of use; OA articles are governed by the applicable Creative Commons License

of the upstream B_Y component and the strength of the solar wind convective electric field (Browett et al., 2017; Case et al., 2018; Rong et al., 2015). During sustained solar wind driving, the B_Y component can become embedded in both the lobe and plasma sheet regions (Newell et al., 1995; Tenfjord et al., 2015), producing twisted magnetic topologies, displaced neutral sheets, and asymmetric magnetic flux distributions between the northern and southern lobes (Cowley, 1981; Lane et al., 2022; Maezawa et al., 1997; Vo et al., 2023). These topological distortions introduce significant north–south asymmetries in the magnetotail structure and plasma flow, generate asymmetric field-aligned current systems, and modulate ionospheric energy deposition and auroral convection patterns (Cao et al., 2014; Chong et al., 2022; Pitkänen et al., 2018, 2024; Taguchi, 1992). In addition, the presence of embedded B_Y modifies the geometry of magnetotail reconnection, transforming it from a symmetric antiparallel configuration into a guide-field regime in which the reconnecting magnetic fields are skewed and non-antiparallel (Ohma et al., 2021). This transition fundamentally alters the onset conditions for reconnection, the efficiency of magnetic energy conversion, and the characteristics of particle acceleration in the magnetotail.

Although the energy and mass pathways in solar wind-magnetosphere coupling have each been extensively investigated, an important unresolved issue is how these two processes are related under different solar wind driving states. In this study, we investigate the magnetotail plasma sheet response, spanning both energy and mass domains, to varying solar wind forcing conditions. Utilizing conjunctional data sets from the upstream OMNI solar wind database and in situ observations from the Magnetospheric Multiscale (MMS) mission, we applied a novel hybrid filter–decision tree model (HFDTM) to partition the plasma sheet ($X < -10\ R_E$, Geocentric Solar Magnetospheric (GSM)) into three regions: the central plasma sheet (CPS), current sheet (CS), and plasma sheet boundary layer (PSBL). To systematically assess how upstream drivers modulate internal magnetospheric dynamics, we classify solar wind conditions into four distinct regimes, based on IMF B_Z polarity and solar wind speed: low-speed northward (LSNW; $|Vx| < 400$ km/s, $B_Z > 0$), low-speed southward (LSSW; $|Vx| < 400$ km/s, $B_Z < 0$), high-speed northward (HSNW; $|Vx| > 400$ km/s, $B_Z > 0$), and high-speed southward (HSSW; $|Vx| > 400$ km/s, $B_Z < 0$). For each regime, we conduct a comprehensive statistical analysis of key parameters, including the convective electric field (E_{CY}), kinetic electric field (E_K), ion density (n_i) and temperature (T_i), and the magnetic field B_Y component, across all 3 PS subregions. Our results reveal a dual-path coupling mechanism between the solar wind and the magnetosphere: strong energy coupling (loading/unloading) under southward IMF, weak coupling (energy relaxation) under northward IMF, and persistent mass loading of the plasma sheet across all solar wind conditions.

2. Data and Partition Method Interpretation

2.1. Data Set Acquisition

Upstream SW and IMF parameters are sourced from the OMNI data set, which provides 1-minute resolution time-shifted solar wind measurements propagated to the Earth's bow shock nose. These measurements offer comprehensive near-Earth monitoring of solar wind conditions, including plasma parameters and IMF orientation. To investigate internal magnetotail dynamics, we utilize survey-mode measurements from NASA's Magnetospheric Multiscale (MMS) mission (Burch et al., 2016), which delivers high-fidelity multi-point observations within the magnetotail. Three key MMS instruments are employed:

1. The Fluxgate Magnetometer (FGM) (Russell et al., 2016), which measures the full vector magnetic field at a cadence of 125 ms (8 Hz), enabling the resolution of mesoscale magnetic structures;
2. The Fast Plasma Investigation suite (Pollock et al., 2016), which continuously samples ion and electron distribution functions at time resolutions of 4.5 s (0.22 Hz), capturing detailed plasma dynamics;
3. The Electric Double Probe (EDP) instrument (Lindqvist et al., 2016), which records electric field components at 7.8 ms (128 Hz) in survey mode, suitable for resolving fast electric field fluctuations.

All MMS and OMNI observations are transformed into the GSM coordinate system to maintain consistency with upstream solar wind vectors and the large-scale orientation of the magnetosphere. The data set spans a five-year period from 2017 to 2021, covering a broad range of solar wind conditions suitable for statistical analysis of plasma sheet dynamics. During this period, a total of 205,476 data points were collected within the near-Earth tail plasma sheet in the range of $X < -10\ R_E$ and $|Y| < 15\ R_E$.

21699402, 2026, 5, Downloaded from https://agupubs.onlinelibrary.wiley.com/doi/10.1029/2025JA034883 by Hui Li - Center For Space Science And Applied Research, CAS , Wiley Online Library on [21/05/2026]. See the Terms and Conditions (https://onlinelibrary.wiley.com/terms-and-conditions) on Wiley Online Library for rules of use; OA articles are governed by the applicable Creative Commons License

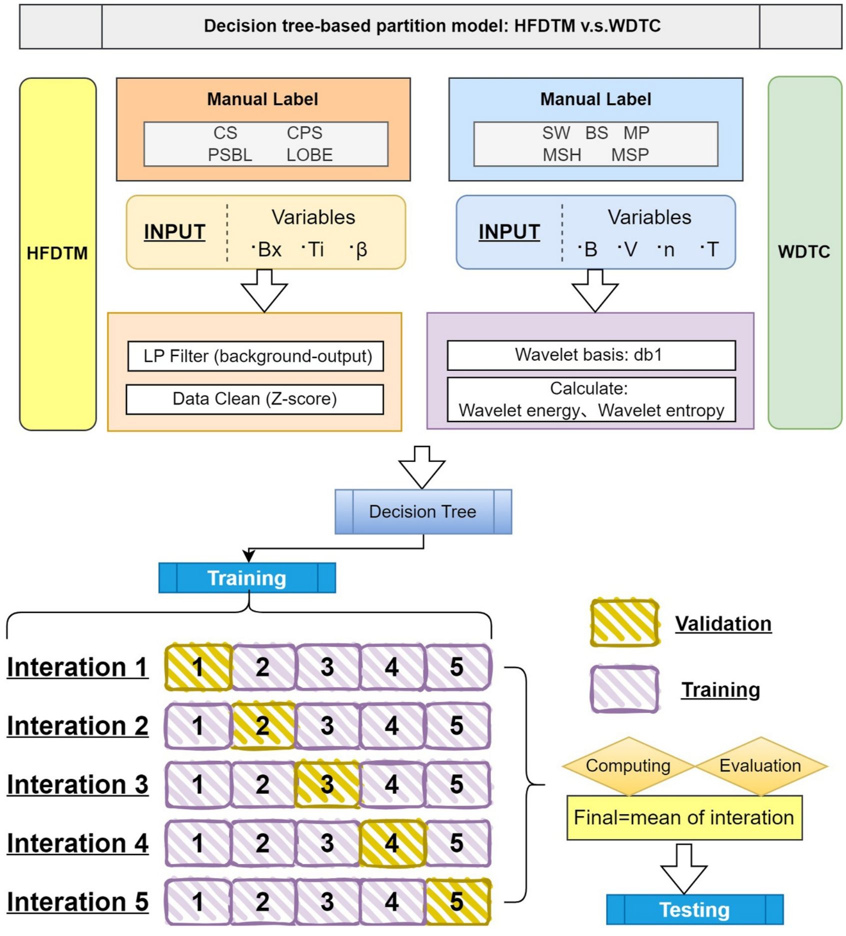

Figure 1. Workflow comparison of the decision tree-based classifiers: HFDTM (left) and Wavelet–Decision Tree Classifier (WDTC) (right). HFDTM applies low-pass filtering and Z-score normalization to nightside MMS data, using B_X, T_i, and β as inputs to classify CS, CPS, plasma sheet boundary layer, and Lobe. WDTC, optimized for the dayside, uses wavelet-based entropy and energy on B, V, T_i, and n to classify SW, BS, MSH, MP, and MSP.

2.2. Filtering Processing

To separate large-scale background fields from superimposed fluctuations associated with wave activity, magnetic reconnection, and plasma turbulence, we applied a second-order Butterworth low-pass filter using MATLAB's butter and filtfilt functions. The filter cutoff frequency is set at 1/600 Hz (equivalent to a 10-minute period), which effectively isolates quasi-static background structures while preserving mesoscale features such as dipolarization fronts, reconnection signatures, and substorm-related injections. This filtering process is applied uniformly to both upstream and in situ data sets, including magnetic field components (B_X, B_Y, B_Z) and ion number density (n). Perturbation quantities are calculated as residuals between the original and filtered time series, defined as ΔB = B_original–B_filtered, Δn = n_original–n_filtered.

Following the filtering process, the continuous time series from both OMNI and MMS data sets are segmented into 1-minute intervals. Each segment is used to compute time-averaged background conditions along with the corresponding perturbations. This segmentation strategy enables a systematic comparison of field coupling behaviors across different plasma regions and solar wind driving regimes.

2.3. Statistical Interpretation

To effectively analyze and visualize the extensive data set comprising 175,601 magnetotail measurements, we employ statistical binning techniques designed to reveal underlying trends while minimizing the influence of

21699402, 2026, 5, Downloaded from https://agupubs.onlinelibrary.wiley.com/doi/10.1029/2025JA034883 by Hui Li - Center For Space Science And Applied Research, CAS , Wiley Online Library on [21/05/2026]. See the Terms and Conditions (https://onlinelibrary.wiley.com/terms-and-conditions) on Wiley Online Library for rules of use; OA articles are governed by the applicable Creative Commons License

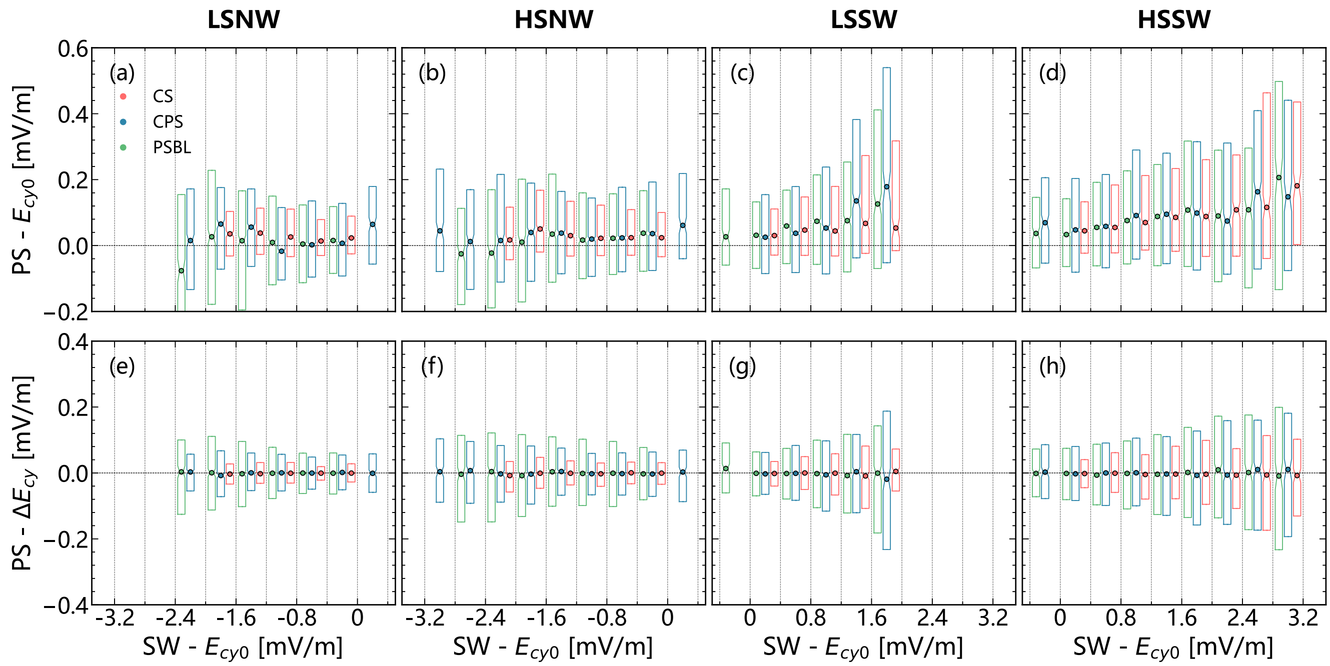

Figure 2. Penetration effect of the steady solar wind dawn-dusk convective electric field (SW–E_{CY0}) into the magnetotail plasma sheet under distinct interplanetary magnetic field (IMF) B_Z and solar wind speed conditions. From left to right, panels are low-speed northward IMF (LSNW), high-speed northward IMF (HSNW), Low-speed southward IMF (LSSW), and high-speed southward IMF (HSSW). Each data point represents the region-averaged value of PS–E_{CY} for a given bin of SW–E_{CY0}. Upper panels show the response of the background component PS–E_{CY0} under (a) LSNW, (b) HSNW, (c) LSSW, and (d) HSSW. Bottom panels show the corresponding perturbation component (PS–ΔE_{CY}) under (e) LSNW, (f) HSNW, (g) LSSW, and (h) HSSW.

short-term variability and outliers. For all 2D box-and-whisker plots (e.g., Figures 2–6), bins are defined along the *X*-axis using a fixed-width scheme, with a minimum of 250 data points per bin to ensure statistical robustness.

2.4. Partition Models: HFDTM Versus WDTC

Recent advances in machine learning have demonstrated the efficacy of decision tree–based classifiers for identifying plasma regions across the Earth's magnetosphere (Wang, Liu, Dai, Zheng, et al., 2025; Wang, Liu, Dai, Jiang, et al., 2025). As illustrated in Figure 1, the Wavelet–Decision Tree Classifier (WDTC) leverages the compressive magnetohydrodynamic (MHD) properties of dayside regions by extracting frequency-localized features via wavelet decomposition. The classifier uses four input variables: total magnetic field strength (B), ion velocity (V), ion temperature (T_i), and plasma density (n). These features are particularly effective in identifying boundary layers where kinetic energy is dissipated through sharp gradients and MHD compressions. Wavelet–Decision Tree Classifier has demonstrated high classification accuracy in delineating key dayside structures, including the SW, bow shock (BS), magnetosheath (MSH), magnetopause (MP), and magnetosphere (MSP) (Wang, Liu, Dai, Zheng, et al., 2025). However, its performance degrades significantly on the nightside, where plasma dynamics become increasingly turbulent, intermittent, and structurally diffuse.

To address these limitations, Wang, Liu, Dai, Jiang, et al. (2025) introduced the hybrid filter–decision tree model (HFDTM), a physically informed machine learning-based classifier specifically optimized for the nightside magnetotail. Rather than employing wavelet-based preprocessing, HFDTM applies a second-order Butterworth low-pass filter to remove high-frequency turbulence and retain mesoscale equilibrium structures. The model targets four fundamental plasma regions: CS, CPS, PSBL, and the lobe. Classification is driven by a minimal yet diagnostically rich feature set consisting of the B_X component of the magnetic field, ion temperature T_i, and plasma beta (β). HFDTM was trained using a manually labeled data set comprising 300 representative events per region, carefully curated through expert selection. Each event was identified based on empirically defined thresholds in magnetic and plasma parameters that capture the distinct physical characteristics of the respective plasma regions. These classification criteria are as follows:

21699402, 2026, 5, Downloaded from https://agupubs.onlinelibrary.wiley.com/doi/10.1029/2025JA034883 by Hui Li - Center For Space Science And Applied Research, CAS , Wiley Online Library on [21/05/2026]. See the Terms and Conditions (https://onlinelibrary.wiley.com/terms-and-conditions) on Wiley Online Library for rules of use; OA articles are governed by the applicable Creative Commons License

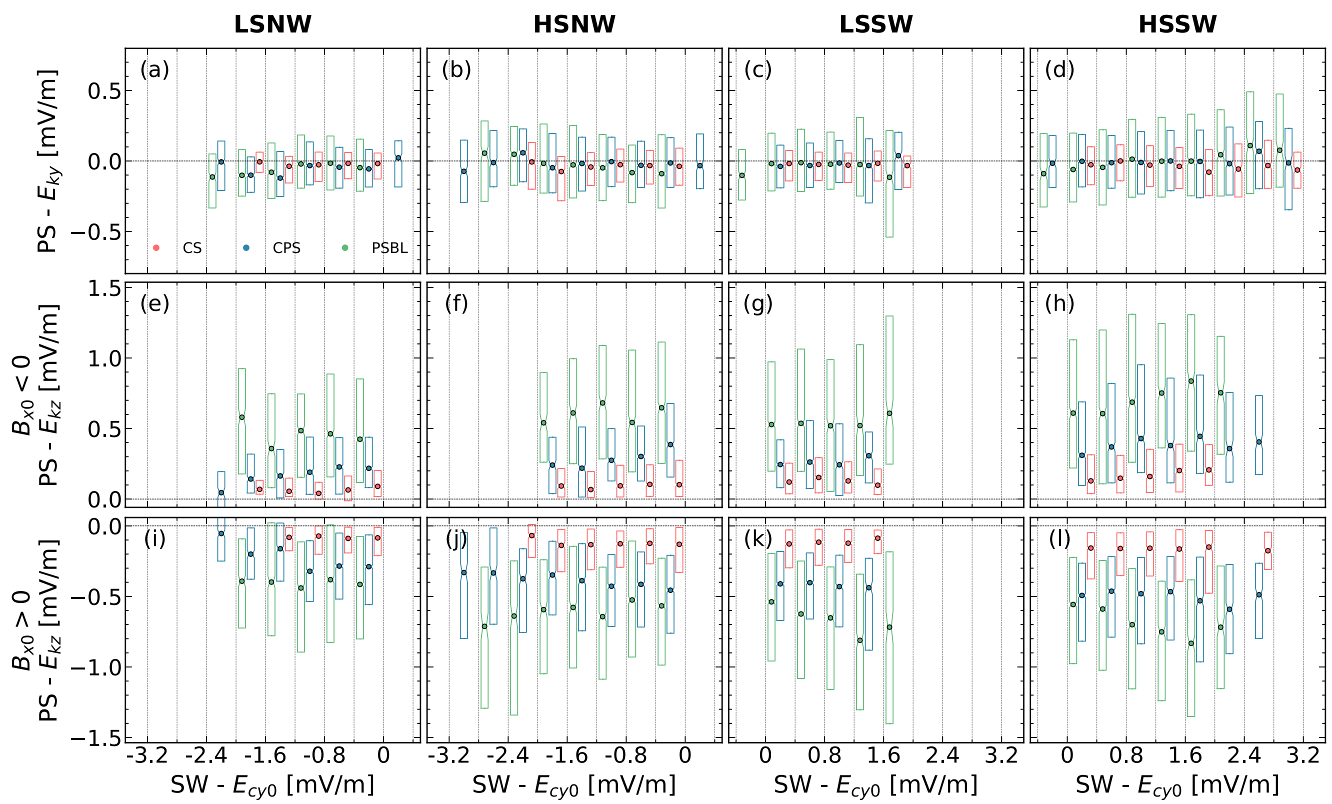

Figure 3. Evolution relationship between the kinetic electric field (E_K) in the plasma sheet and solar wind background convective electric field ($SW–E_{CY0}$) across four interplanetary magnetic field and solar wind regimes. The top row presents the dawn–dusk component of E_K ($PS–E_{KY}$), while the middle and bottom rows show the normal component ($PS–E_{KZ}$) in the southern ($Bx < 0$) and northern ($Bx > 0$) hemispheres, respectively. Upper panels show the response of the $PS–E_Y$ under (a) LSNW, (b) HSNW, (c) LSSW, and (d) HSSW. Middle panels show the corresponding response of $PS–E_Z$ under $Bz < 0$ conditions for (e) LSNW, (f) HSNW, (g) LSSW, and (h) HSSW. Bottom panels show the response of $PS–E_Z$ under $Bz > 0$ conditions for (i) LSNW, (j) HSNW, (k) LSSW, and (l) HSSW.

1. CS: $|Bx| < 5$ nT, $T_i > 2$ keV, and $\beta > 5$;
2. CPS: 5 nT $\leq |Bx| < 15$ nT, Ti > 1 keV, and $\beta \sim 1$;
3. PSBL: $15 \leq |Bx| < 25$ nT, $T_i \sim 0.5–2$ keV, and $\beta \sim 0.1–0.5$;
4. Lobe: $|Bx| > 25$ nT, $T_i < 0.1$ keV, and $\beta < 0.1$.

These empirically derived parameter ranges guided both the labeling of the training data set and the interpretation of classification boundaries, allowing for physically consistent and high-resolution identification of plasma sheet substructures. The model thus achieves robust performance in distinguishing magnetotail plasma regions, enhancing the interpretability and physical relevance of machine learning–based classification in space plasma studies.

3. Statistical Results

3.1. E-Penetration (Energy Channel)

The dawn–dusk convective electric field in the solar wind ($SW–E_{CY}$) serves as a major energy driver for magnetospheric dynamics, encapsulating the cross-magnetospheric potential. To evaluate energy transmission into the plasma sheet, we consider a 10-minute time lag between the upstream $SW–E_{CY}$ and the internal plasma sheet electric field ($PS–E_{CY}$), consistent with previous estimates of flux tube convection timescales (Nishimura et al., 2009; Snekvik et al., 2017). Only the background component of the solar wind electric field ($SW–E_{CY0}$) is analyzed here, as it represents the steady-state external driving potential. Within the plasma sheet, the convection electric field ($PS–E_{CY}$), calculated as $-V_{PS} \times B_{PS}$, is decomposed into two components: a background (global) component ($PS–E_{CY0}$) and a perturbation (local) component ($\Delta E_{CY} = E_{CY} - E_{CY0}$). The background component captures the quasi-static structure of large-scale convection, while the perturbation component reflects transient

21699402, 2026, 5, Downloaded from https://agupubs.onlinelibrary.wiley.com/doi/10.1029/2025JA034883 by Hui Li - Center For Space Science And Applied Research, CAS , Wiley Online Library on [21/05/2026]. See the Terms and Conditions (https://onlinelibrary.wiley.com/terms-and-conditions) on Wiley Online Library for rules of use; OA articles are governed by the applicable Creative Commons License

electric field variations linked to mesoscale processes. This separation enables a more nuanced examination of both global energy transport and localized dynamical activity within the plasma sheet.

Figure 2 presents box-and-whisker plots comparing the upstream SW–E_{CY0} with PS–E_{CY0} (top panels) and ΔE_{CY} (bottom panels) across four distinct upstream regimes. The PS–E_{CY0} values exhibit a clear and systematic dependence on upstream solar wind driving conditions. Under SWIMF conditions, PS–E_{CY0} shows a consistent and monotonic increase with rising SW–E_{CY0} across all three PS regions, reflecting strong upstream–downstream energy coupling. In contrast, under NWIMF, this relationship becomes ambiguous, characterized by more scattered responses and weaker trends, indicating reduced sensitivity to upstream driving. Overall, PS–E_{CY0} values are stronger and more positively correlated with SW–E_{CY0} during LSSW and HSSW (Panels c and d), while correlations under LSNW and HSNW (Panels a and b) are weaker. This pattern is consistent with diminished dayside reconnection and suppressed global convection under northward IMF, which reduces the efficiency of solar wind energy transfer into the magnetosphere.

The perturbation component (ΔE_{CY}, bottom row) shows a weak correlation with SW–E_{CY0} across all four upstream regimes. In LSNW, HSNW, and LSSW (Panels e–g), ΔE_{CY} amplitudes (box height) remain relatively small, typically within ±0.05 mV/m, with distributions centered near zero and only minor variations in shape and skewness across regions. In HSSW (Panel h), the amplitude spread increases, especially in the CPS and PSBL regions, suggesting stronger magnetotail activities. These fluctuations are primarily associated with magnetotail processes, such as magnetic reconnection, bursty bulk flows (BBFs), and magnetic dipolarization, rather than with large-scale solar wind driving.

3.2. E_K-Behavior (Energy Dissipation)

To complement the analysis of the convective electric field, we examine the kinetic electric field (E_K), which captures contributions from wave activity, Hall effects, and other non-convective processes not described by the ideal MHD convection field. E_k is defined as the non-convective component of the electric field, calculated as: $E_K = E-(-V_i \times B)$, where E is the measured electric field from MMS/EDP, and Vi and B are the ion velocity and magnetic field, respectively.

Figure 3 presents box-and-whisker plots of the dawn–dusk (E_{KY}) component (top row) and the normal (E_{KZ}) component (middle and bottom rows) plotted against upstream solar wind driving (SW–E_{CY}) across the four IMF regimes. Across all regimes, PS–E_{KY} amplitudes remain relatively weak, typically within ±0.2 mV/m. The distributions are widely scattered, and no consistent correlation with SW–E_{CY} is observed. This suggests that the E_K is largely decoupled from steady solar wind driving. Corresponding correlation coefficients are generally low in the CS and CPS. PSBL occasionally exhibits higher correlations, but their signs vary across regimes, indicating the absence of a consistent trend and highlighting regime-dependent variability.

To investigate hemispheric symmetry in the vertical electric field (E_{KZ}), the data are partitioned by B_X polarity, which approximates hemispheric mapping. Panels (e–h) correspond to $B_{X0} < 0$ (Southern Hemisphere), while Panels (i–l) correspond to $B_{X0} > 0$ (Northern Hemisphere). The resulting distributions reveal striking hemispheric symmetry: E_{KZ} is predominantly positive in the Southern Hemisphere and negative in the Northern Hemisphere, indicating a consistently equatorward E_{KZ} in both hemispheres. This spatial pattern aligns with the expected Hall electric field structure generated during collisionless magnetic reconnection, where ion–electron decoupling gives rise to localized Hall fields, especially pronounced in the PSBL.

As shown in Figure 3, the variability of E_K follows the ordering HSSW > LSSW > HSNW > LSNW, indicating that E_K fluctuations systematically increase with solar wind driving strength. This result suggests that, although E_K fluctuations arise from magnetotail processes such as magnetic reconnection and associated dynamics, the intensity of these processes is strongly regulated by upstream solar wind conditions. Stronger solar wind driving therefore leads to enhanced magnetotail activity and consequently larger E_K fluctuations.

3.3. n-Penetration (Mass Channel)

Figure 4 presents a statistical analysis of ion density penetration from the solar wind into the magnetotail plasma sheet by comparing the solar wind ion density (SW–n_i) with the plasma sheet (PS–n_i) (in log-log coordinates). To isolate the large-scale mass-loading trend from short-term fluctuations, a background filtering procedure was applied to PS–n_i, thereby suppressing transient variability and emphasizing systematic coupling behavior. Across

21699402, 2026, 5, Downloaded from https://agupubs.onlinelibrary.wiley.com/doi/10.1029/2025JA034883 by Hui Li - Center For Space Science And Applied Research, CAS , Wiley Online Library on [21/05/2026]. See the Terms and Conditions (https://onlinelibrary.wiley.com/terms-and-conditions) on Wiley Online Library for rules of use; OA articles are governed by the applicable Creative Commons License

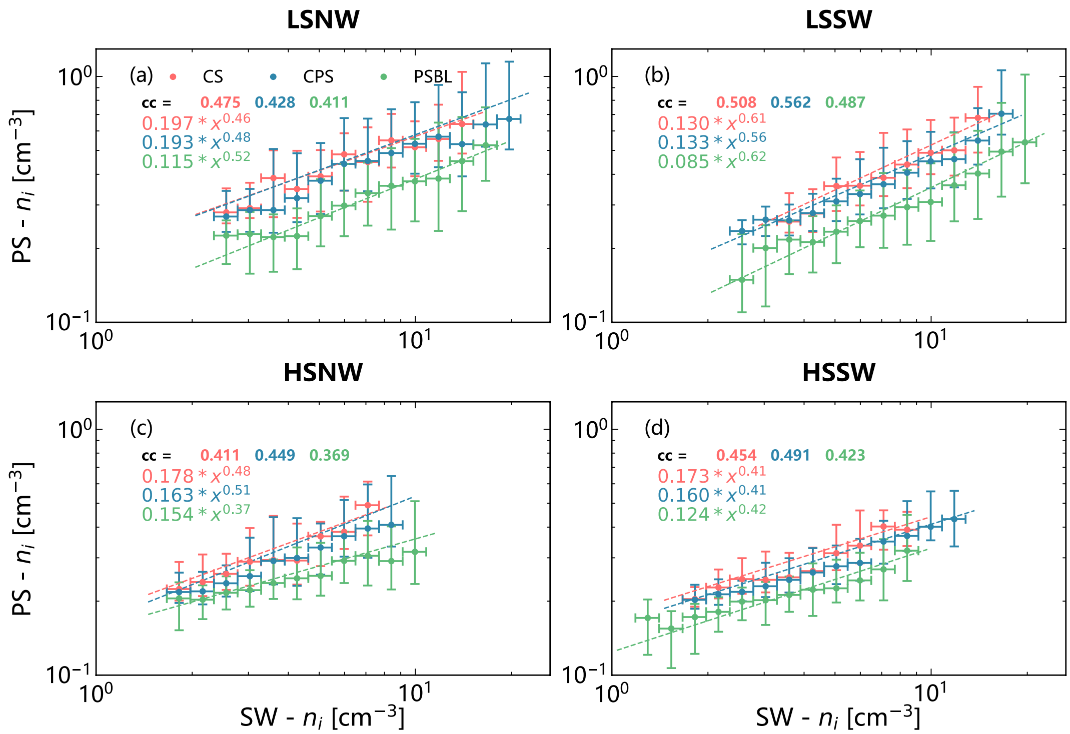

Figure 4. Statistical relationship between solar wind ion density (SW−n_i) and plasma sheet ion density (PS−n_i) derived from the full MMS data set under four upstream driving conditions: (a) LSNW, (b) LSSW, (c) HSNW, and (d) HSSW. PS–n_i is background-filtered to suppress short-term fluctuations and emphasize large-scale mass-loading trends. Colored symbols represent different plasma sheet regions (CS, CPS, and plasma sheet boundary layer), and dashed lines denote power-law fits shown in log-log coordinates. The correlation coefficient (CC) and the power-law scaling relation PS–n_i = A(SW–n_i)^K, where K represents the scaling exponent, are listed in each panel. All quantitative values are calculated using the full set of available MMS observations.

all regimes, SW–n_i and PS–n exhibit consistent positive correlations, demonstrating that solar-wind density variations are directly reflected in plasma sheet density. A clear spatial hierarchy is also evident: ion densities in the CS and CPS remain closely aligned and systematically higher than those in the PSBL, suggesting that solar-wind-origin plasma preferentially accumulates in the central plasma sheet. However, the correlation coefficients (CC = 0.37–0.56) indicate moderate correlations, implying that while mass transport is robust and persistent, it is highly modulated by internal magnetotail dynamics, mixing, and transport variability.

Under low-speed northward IMF conditions (LSNW; Figure 4a), the correlations are moderate in CS (CC = 0.475) and weaker in the CPS (CC = 0. 428) and PSBL (CC = 0. 411). The corresponding fitted exponents are $K \approx 0.46$ in the CS, 0.48 in the CPS and 0.52 in PSBL. These values indicate a sublinear response of plasma sheet density to increasing solar wind density, with a slightly stronger scaling toward the outer plasma sheet region. In low-speed southward IMF conditions (LSSW; Figure 4b), the coupling strengthens slightly, particularly in CPS (CC = 0.562), while CS remains similar (CC = 0.508) and PSBL again shows weaker correlation (CC = 0. 487). Slopes are comparable across regions ($K \approx$ 0.56–0.62), indicating a relatively uniform mass penetration efficiency during low-speed solar wind intervals.

For high-speed northward IMF conditions (HSNW; Figure 4c), the correlations weaken slightly, with CC values of 0.411 in the CS, 0.449 in the CPS, and 0.369 in the PSBL. The fitted exponents are $K = 0.48$ in the CS, 0.51 in the CPS, and 0.37 in the PSBL. These results indicate that the positive SW–PS density relationship remains present, but the response becomes weaker in the PSBL, suggesting greater transport variability or reduced penetration efficiency in the boundary layer under high-speed northward conditions. In high-speed southward IMF conditions (HSSW; Figure 4d), the correlations remain moderate, with CC values of 0.454 in the CS, 0.491 in the CPS, and 0.423 in the PSBL. The corresponding exponents are K = 0.41, 0.41, and 0.42, respectively. Compared with LSSW, the smaller and more uniform K values suggest that although mass loading remains

21699402, 2026, 5, Downloaded from https://agupubs.onlinelibrary.wiley.com/doi/10.1029/2025JA034883 by Hui Li - Center For Space Science And Applied Research, CAS , Wiley Online Library on [21/05/2026]. See the Terms and Conditions (https://onlinelibrary.wiley.com/terms-and-conditions) on Wiley Online Library for rules of use; OA articles are governed by the applicable Creative Commons License

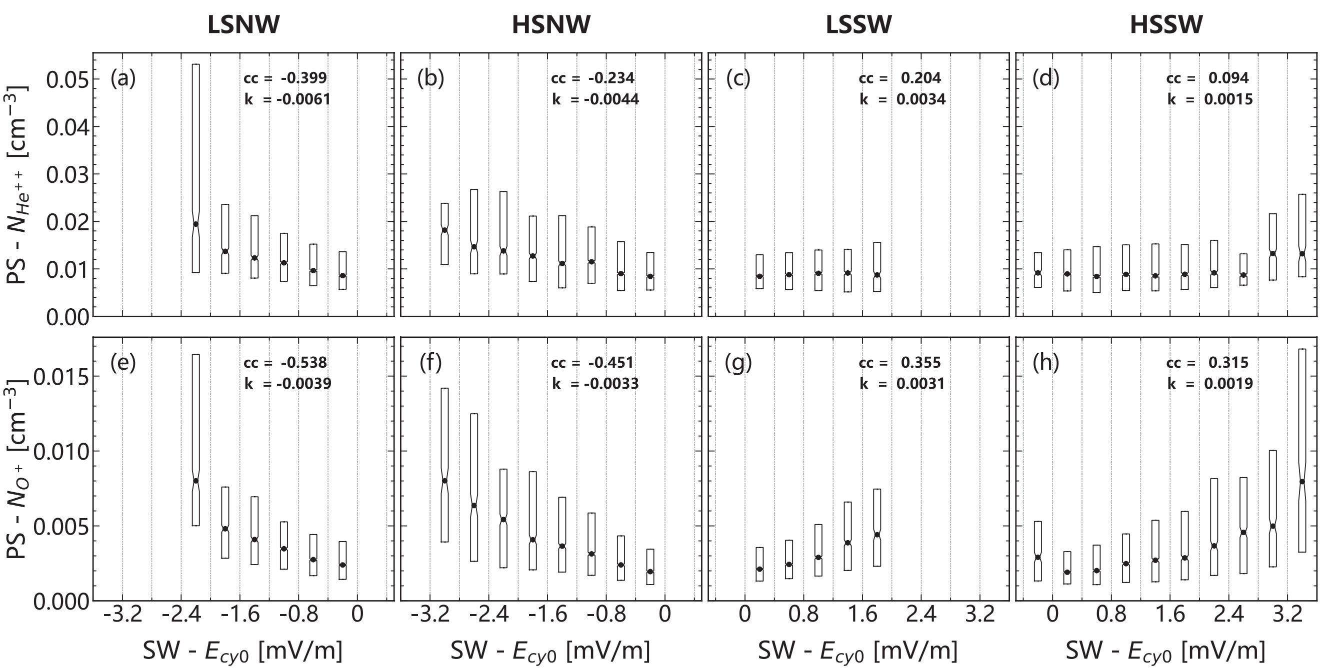

Figure 5. Distribution of He^{++} and O^+ ion densities in the plasma sheet (PS) as a function of the solar wind electric field component E_{CY0} under four upstream solar wind conditions: low-speed northward interplanetary magnetic field (IMF) (LSNW), high-speed northward IMF (HSNW), low-speed southward IMF (LSSW), and high-speed southward IMF (HSSW). Panels (a–d) show the PS density of solar wind–originating He^{++} ions and panels (e–h) show the PS density of ionospheric O^+ ions. The horizontal axis in all panels denotes the solar wind electric field E_{CY0} (mV/m).

effective, the density response to upstream solar wind variations becomes weaker and more spatially homogeneous under stronger solar wind driving.

3.4. Source Attribution: Solar Wind Versus Ionospheric Contributions

To evaluate the relative contributions of solar wind and ionospheric sources to plasma sheet mass loading, Figure 5 examines the behavior of He^{++} and O^+ ion densities, representative tracers of solar wind and ionospheric origin, respectively, under four distinct upstream regimes. Panels (a)–(d) show the variation of He^{++} density (n_He^{++}) as a function of the upstream convective electric field (SW–E_{CY0}).

Under northward IMF conditions (LSNW and HSNW), weak-to-moderate negative correlations were obtained (LSNW: CC = −0.399, $K = -0.0061$; HSNW: CC = −0.234, $K = -0.0044$). Importantly, Both CC and absolute magnitude of the slope |K| are larger during northward IMF compared with southward IMF (LSSW: CC = 0.204, $K = 0.0034$; HSSW: CC = 0.094, $K = 0.0015$), indicating that solar-wind-origin heavy-ion density is actually more sensitive to variations in convective electric field under northward IMF conditions.

Lower panels (e)–(h) show the distribution of O^+ density (PS–n_{O+}), a key tracer of ionospheric outflow. Similar to He^{++}, northward IMF regimes exhibit larger absolute slopes (LSNW: CC = −0.538, $K = -0.0039$; HSNW: CC = −0.451, $K = -0.0033$) compared with southward IMF regimes (LSSW: CC = 0.355, $K = 0.0031$; HSSW: CC = 0.315, $K = 0.0019$). Again, the larger |K| under northward IMF indicates enhanced sensitivity of ionospheric plasma transport to convection changes when reconnection-driven energy input is reduced. The combined behavior of He^{++} and O^+ in n Figure 5 demonstrates that although IMF orientation governs the global convection framework, the compositional response of both solar-wind-origin and ionospheric-origin ions becomes more pronounced under northward IMF conditions, highlighting the increasing importance of transport and plasma supply processes during weaker reconnection states.

3.5. B_Y-Penetration: Modulation Structure

To evaluate how the IMF B_Y modulates the large-scale structure of the magnetotail, Figure 6 presents regime-separated scatter plots of plasma sheet B_Y (PS–B_{Y0}) versus upstream solar wind B_Y (SW–B_{Y0}), using a

21699402, 2026, 5, Downloaded from https://agupubs.onlinelibrary.wiley.com/doi/10.1029/2025JA034883 by Hui Li - Center For Space Science And Applied Research, CAS , Wiley Online Library on [21/05/2026]. See the Terms and Conditions (https://onlinelibrary.wiley.com/terms-and-conditions) on Wiley Online Library for rules of use; OA articles are governed by the applicable Creative Commons License

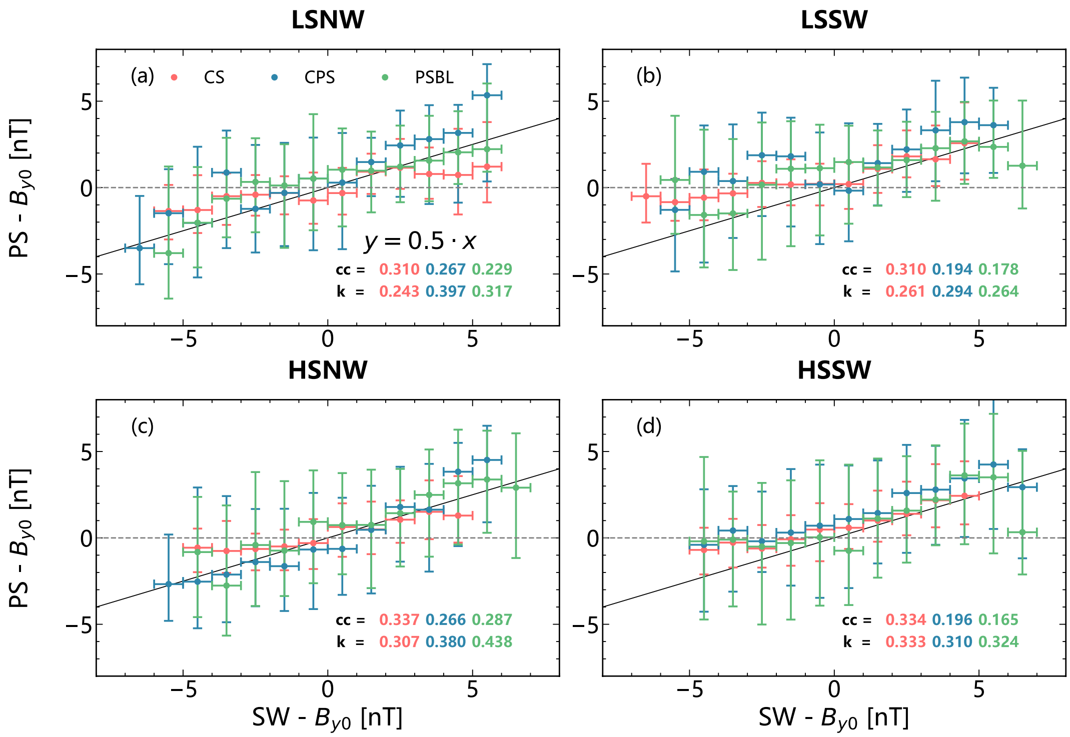

Figure 6. Penetration of the solar wind B_Y component into different tail plasma regions of the magnetotail under varying solar wind and interplanetary magnetic field (IMF) conditions. Panels (a–d) correspond to Low-speed northward IMF (LSNW), Low-speed southward IMF (LSSW), high-speed northward IMF (HSNW), and high-speed southward IMF (HSSW), respectively. The horizontal axis represents the strength of the solar wind B_Y in the background field (SW−B_{Y0}), while the vertical axis shows the corresponding B_Y strength in the plasma sheet (PS−B_{Y0}). The solid line in each panel is the reference line with a slope of 0.5, representing 50% transmission efficiency.

60-minute lag to account for transmission delays. This time threshold follows previous studies by Rong et al. (2015) and Tenfjord et al. (2018), which demonstrated that delayed response in PS-B_{Y0} is indictive of large-scale IMF B_Y penetration into the magnetotail.

Under low-speed northward IMF (LSNW; panel a), all three regions exhibit a clear positive trend. The CS shows CC = 0.310 with $K = 0.243$, while the CPS and PSBL display CC = 0.267 and 0.229 with larger slopes of $K = 0.397$ and $K = 0.317$, respectively. Despite low/moderate correlations, the consistent positive slopes indicate that IMF B_Y penetration persists even during weak solar wind driving, suggesting that a relatively stable magnetotail configuration allows upstream asymmetry to propagate into both the central plasma sheet and its

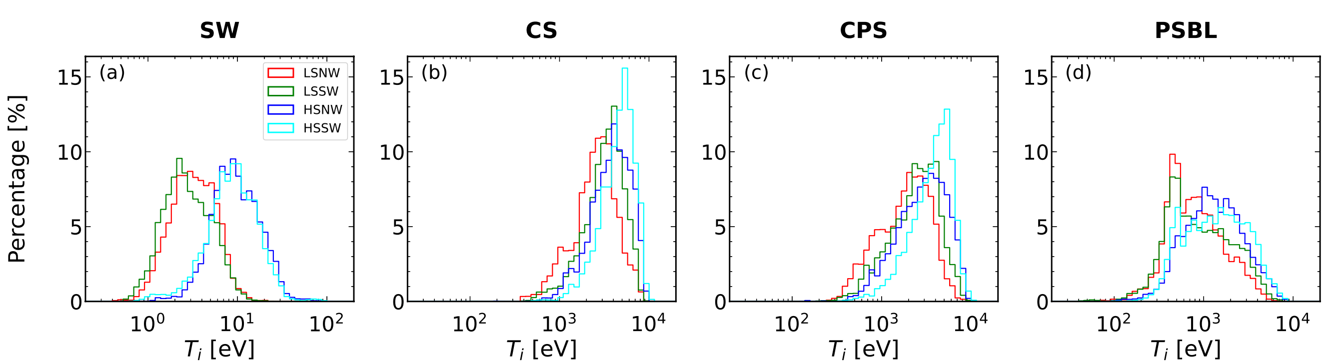

Figure 7. Histograms of background ion temperature (T_i) distributions in the solar wind and different regions of the magnetotail plasma sheet under four solar wind driving conditions. Panels (a–d) display the probability density functions of T_i in the solar wind, tail current sheet, center plasma sheet, and plasma sheet boundary layer, respectively. The ion temperatures were plotted on a logarithmic scale along the *X*-axis.

21699402, 2026, 5, Downloaded from https://agupubs.onlinelibrary.wiley.com/doi/10.1029/2025JA034883 by Hui Li - Center For Space Science And Applied Research, CAS , Wiley Online Library on [21/05/2026]. See the Terms and Conditions (https://onlinelibrary.wiley.com/terms-and-conditions) on Wiley Online Library for rules of use; OA articles are governed by the applicable Creative Commons License

21699402, 2026, 5, Downloaded from https://agupubs.onlinelibrary.wiley.com/doi/10.1029/2025JA034883 by Hui Li - Center For Space Science And Applied Research, CAS , Wiley Online Library on [21/05/2026]. See the Terms and Conditions (https://onlinelibrary.wiley.com/terms-and-conditions) on Wiley Online Library for rules of use; OA articles are governed by the applicable Creative Commons License

boundary layers. During low-speed southward IMF (LSSW; panel b), the penetration pattern becomes more dispersed. Correlations decrease slightly in the CPS (CC = 0.194) and PSBL (CC = 0.178), while the CS remains at CC = 0.310. Slopes remain comparable across regions ($K \approx 0.261$–0.294), indicating that IMF B_Y penetration continues but with increased variability, likely associated with enhanced reconnection-driven restructuring. In contrast, high-speed northward IMF (HSNW; panel c) shows relatively large-scale behavior. CS exhibits CC = 0.337 with $K = 0.307$, while the CPS and PSBL display CC = 0.266 and 0.287 with larger slopes of $K = 0.380$ and $K = 0.438$, respectively. Under high-speed southward IMF (HSSW; panel d), IMF B_Y penetration remains evident but regionally decreases. The CS maintains the strongest correlation (CC = 0.334), followed by the CPS (0.196) and PSBL (0.165), while slopes remain moderate ($K = 0.333$, 0.310, and 0.324, respectively).

3.6. Ion Temperature: SW Versus PS

Figure 7 displays the probability density distributions of ion temperature (T_i) in the upstream solar wind (Panel a) and within three distinct regions of the magnetotail plasma sheet: CS (Panel b), CPS (Panel c), and PSBL (Panel d), under four distinct solar wind regimes. In the upstream solar wind, the distributions show a clear dependence on solar wind speed. High-speed regimes (HSNW and HSSW) are characterized by elevated ion temperatures, peaking near 10 eV, while low-speed regimes (LSNW and LSSW) show peaks near 1–3 eV. The observed monotonic relationship between T_i and solar wind speed suggests that upstream thermal properties are well preserved throughout the solar wind's heliospheric journey.

Once inside the magnetotail, however, this upstream ordering breaks down. Across the CS, CPS, and PSBL (panels b–d), T_i distributions adopt similar unimodal shapes that consistently peak between 10^3 and 10^4 eV, regardless of the upstream regime. This convergence indicates that ion heating within the magnetotail is predominantly controlled by internal magnetospheric mechanisms rather than direct inheritance from upstream solar wind temperatures. The strong consistency in both distribution shape and peak energy across regions and driving conditions points to the operation of universal energization mechanisms within the plasma sheet, potentially including magnetic reconnection, stochastic heating, and wave–particle interactions (Zhang, Wang, Dai, Baumjohann et al., 2022; Zhang, Wang, Dai, Ren et al., 2022). Collectively, these observations highlight the magnetotail as a primary site of energy conversion, where incoming solar-wind energy is redistributed and transformed through complex tail dynamics.

4. Discussion

Borovsky et al. (1998) examined solar wind–plasma sheet coupling using simultaneous observations from spacecraft positioned in both the upstream solar wind and the magnetotail plasma sheet. By combining 5-minute averaged ISEE-3 solar wind data and 1-hour OMNI data from IMP-8 with high-resolution (3–12 s) ISEE-2 plasma sheet measurements, they identified several key statistical relationships: (a) a weak correlation between plasma sheet E_Y and solar wind E_Y; (b) a strong correlation between plasma sheet ion density and solar wind density; and (c) a significant correlation between PS B_Y and IMF B_Y, with a reported B_Y penetration factor of about 76%.

In contrast to that earlier framework, our study goes beyond bulk statistical comparison by separating quasi-static background components from mesoscale fluctuations. This decomposition reveals that the background convection electric field, PS–E_{CY0}, which represents the large-scale cross-tail potential associated with dayside reconnection and Dungey-cycle convection, is systematically enhanced under southward IMF conditions, especially during high-speed solar wind intervals. Under northward IMF, the PS–E_{CY0} response becomes more dispersed, indicating reduced reconnection efficiency and a stronger modulation by the internal magnetotail configuration.

Our results also refine our understanding of plasma sheet mass loading. Figure 4 shows that plasma sheet density remains positively correlated with solar wind density under all four solar wind regimes, confirming the robustness of solar wind control on plasma supply. However, the relationship is not simply linear. Instead, it is better characterized as moderate, sublinear, and region dependent. The central sheet and central plasma sheet generally exhibit stronger and more coherent coupling than the PSBL, while both IMF orientation and solar wind speed influence the correlation strength and the fitted exponent K. This extends previous work by showing that solar wind–plasma sheet mass coupling depends not only on upstream density but also on plasma sheet location and solar wind regime.

21699402, 2026, 5, Downloaded from https://agupubs.onlinelibrary.wiley.com/doi/10.1029/2025JA034883 by Hui Li - Center For Space Science And Applied Research, CAS , Wiley Online Library on [21/05/2026]. See the Terms and Conditions (https://onlinelibrary.wiley.com/terms-and-conditions) on Wiley Online Library for rules of use; OA articles are governed by the applicable Creative Commons License

In addition, Figure 6 demonstrates that IMF B_Y persistently modulates the magnetotail structure across all solar wind categories, but with clear regime dependence. The fitted slopes indicate stronger B_Y penetration under northward IMF than under southward IMF, and under high-speed solar wind compared with low-speed conditions. This suggests that large-scale magnetic asymmetry is transmitted more efficiently when the magnetotail is relatively stable, as under northward IMF, and when convection is stronger, as under high-speed solar wind. By contrast, enhanced reconnection and stronger internal variability during southward IMF broaden the distributions and reduce the apparent efficiency of upstream B_Y transmission into the plasma sheet (Schödel et al., 2001).

These results support a scale-dependent dual-pathway framework for solar wind–magnetosphere coupling. In this picture, the energy pathway is represented by large-scale convective electric-field penetration, which is primarily controlled by reconnection and transports electromagnetic energy along magnetic flux tubes, whereas small-scale kinetic electric fields are more closely linked to internal magnetotail activity and local energy dissipation. The mass pathway, in contrast, is primarily transport driven, reflecting plasma supply from both the solar wind and ionospheric outflow. Within this framework, magnetic-field penetration is more appropriately interpreted as part of the energy pathway rather than the mass pathway, because IMF B_Y transmission reflects large-scale magnetic-flux transport and frozen-in electromagnetic coupling rather than direct plasma supply. At the same time, such magnetic penetration can indirectly influence plasma transport by modifying magnetotail topology, dawn–dusk asymmetry, and drift geometry.

5. Conclusions

In this study, we investigated the dual-channel response of the magnetotail plasma sheet to solar-wind forcing using MMS observations combined with OMNI data from 2017 to 2021. By separating background and perturbation components of key parameters, we quantified how energy transfer, mass loading, and magnetic structure respond to upstream conditions. The results show that energy coupling is strongly IMF dependent: the background convection electric field in the plasma sheet increases systematically with upstream driving under southward IMF, but becomes weaker and more dispersed under northward IMF. In contrast, plasma-sheet ion density remains positively correlated with solar-wind density under all regimes, indicating that mass loading is a persistent feature of solar wind–magnetotail coupling. We also find that IMF B_Y continuously modulates the magnetotail structure, with stronger penetration under northward IMF and during high-speed solar wind. These results support a scale-dependent dual-pathway framework for solar wind–magnetosphere coupling: an electromagnetic energy pathway that is strongly controlled by reconnection and IMF orientation, and a mass-transport pathway that remains active across diverse solar-wind conditions.

Conflict of Interest

The authors declare no conflicts of interest relevant to this study.

Availability Statement

The MMS data sets analyzed during the current study are available in the [CDAWEB] repository https://cdaweb.gsfc.nasa.gov/pub/data/mms/. The OMNI data were obtained from GSFC/SPDF OMNIWeb (http://omniweb.gsfc.nasa.gov). Data analysis was performed using the IRFU-Matlab library (https://github.com/irfu/irfu-matlab).

Acknowledgments

We would like to thank the PIs and those who contributed to the success of the MMS mission. Project Supported by the Specialized Research Fund for State Key Laboratory of Solar Activity and Space Weather. This work is supported by NNSFC Grants (42374198, 42188101) and the project of Civil Aerospace "14th Five Year Plan" Preliminary Research in Space Science (D010301, D010202). H. Li is also supported by the International Partnership Program of CAS (Grant. 183311KYSB20200017).

References

Antonova, E. E., & Ovchinnikov, I. L. (1999). Magnetostatically equilibrated plasma sheet with developed medium-scale turbulence: Structure and implications for substorm dynamics. *Journal of Geophysical Research*, *104*(A8), 17289–17297. https://doi.org/10.1029/1999JA900141

Antonova, E. E., & Ovchinnikov, I. L. (2001). The model of turbulent plasma sheet during IMF Bz > 0. *Advances in Space Research*, *28*(12), 1747–1752. https://doi.org/10.1016/s0273-1177(01)00541-5

Axford, W. I., & Hines, C. O. (1964). A unifying theory of high-latitude geophysical phenomena and geomagnetic storms. *Planetary and Space Science*, *12*(1), 45–64. https://doi.org/10.1016/0032-0633(64)90067-4

Baker, D., Klimas, A., & Vassiliadis, D. (2007). Nonlinear dynamics in the Earth's magnetosphere. In *Nonlinear dynamics in geosciences*. Springer. https://doi.org/10.1007/978-0-387-34918-3_4

Baker, D. N., Pulkkinen, T. I., Angelopoulos, V., Baumjohann, W., & McPherron, R. L. (1996). Neutral line model of substorms: Past results and present view. *Journal of Geophysical Research*, *101*(A6), 12975–13010. https://doi.org/10.1029/95JA03753

Baker, D. N., Zwickl, R. D., Bame, S. J., Hones Jr, E. W., Tsurutani, B. T., Smith, E. J., & Akasofu, S.-I. (1983). An Isee 3 high time resolution study of interplanetary parameter correlations with magnetospheric activity. *Journal of Geophysical Research*, *88*(A8), 6230–6242. https://doi.org/10.1029/JA088iA08p06230

21699402, 2026, 5, Downloaded from https://agupubs.onlinelibrary.wiley.com/doi/10.1029/2025JA034883 by Hui Li - Center For Space Science And Applied Research, CAS , Wiley Online Library on [21/05/2026]. See the Terms and Conditions (https://onlinelibrary.wiley.com/terms-and-conditions) on Wiley Online Library for rules of use; OA articles are governed by the applicable Creative Commons License

Baumjohann, W., Hesse, M., Kokubun, S., Mukai, T., Nagai, T., & Petrukovich, A. A. (1999). Substorm dipolarization and recovery. *Journal of Geophysical Research*, *104*(A11), 24995–25000. https://doi.org/10.1029/1999JA900282

Baumjohann, W., Paschmann, G., & Nagai, T. (1992). Thinning and expansion of the substorm plasma sheet. *Journal of Geophysical Research*, *97*(A11), 17173–17175. https://doi.org/10.1029/92JA01519

Borovsky, J. E., & Bonnell, J. (2001). The dc electrical coupling of flow vortices and flow channels in the magnetosphere to the resistive ionosphere. *Journal of Geophysical Research*, *106*(A12), 28967–28994. https://doi.org/10.1029/1999JA000245

Borovsky, J. E., Elphic, R. C., Funsten, H. O., & Thomsen, M. F. (1997). The Earth's plasma sheet as a laboratory for flow turbulence in high-β MHD. *Journal of Plasma Physics*, *57*, 1–34. https://doi.org/10.1017/S0022377896005259

Borovsky, J. E., Thomsen, M. F., & Elphic, R. C. (1998). The driving of the plasma sheet by the solar wind. *Journal of Geophysical Research*, *103*(A8), 17617–17639. https://doi.org/10.1029/97JA02986

Browett, S. D., Fear, R. C., Grocott, A., & Milan, S. E. (2017). Timescales for the penetration of IMF by into the Earth's magnetotail. *Journal of Geophysical Research: Space Physics*, *122*(1), 579–593. https://doi.org/10.1002/2016JA023198

Burch, J., Moore, T., Torbert, R., & Giles, B. (2016). Magnetospheric multiscale overview and science objectives. *Space Science Reviews*, *199*(1–4), 5–21. https://doi.org/10.1007/s11214-015-0164-9

Cao, J. B., Duan, A., Dunlop, M., Wei, X., & Cai, C. (2014). Dependence of IMF by penetration into the neutral sheet on IMF Bz and geomagnetic activity. *Journal of Geophysical Research: Space Physics*, *119*(7), 5279–5285. https://doi.org/10.1002/2014JA019827

Case, N. A., Grocott, A., Martin, C. J., Haaland, S., & Nagai, T. (2018). Response of Earth's neutral sheet to reversals in the IMF by component. *Journal of Geophysical Research: Space Physics*, *123*(10), 8206–8218. https://doi.org/10.1029/2018JA025712

Chong, G. S., Pitkänen, T., Hamrin, M., & Kullen, A. (2022). Dawn-dusk ion flow asymmetry in the plasma sheet: Interplanetary magnetic field by versus distance with respect to the neutral sheet. *Journal of Geophysical Research: Space Physics*, *127*(4), e2021JA030208. https://doi.org/10.1029/2021JA030208

Cowley, S. W. H. (1981). Magnetospheric asymmetries associated with the y-component of the IMF. *Planetary and Space Science*, *29*(1), 79–96. https://doi.org/10.1016/0032-0633(81)90141-0

Dungey, J. W. (1961). Interplanetary magnetic fields and the auroral zones. *Physical Review Letters*, *6*(2), 47–48. https://doi.org/10.1103/PhysRevLett.6.47

Eastwood, J. P., Hietala, H., Toth, G., Phan, T. D., & Fujimoto, M. (2015). What controls the structure and dynamics of Earth's magnetosphere? *Space Science Reviews*, *188*(1–4), 251–286. https://doi.org/10.1007/s11214-014-0050-x

Fujimoto, M., Terasawa, T., Mukai, T., Saito, Y., Yamamoto, T., & Kokubun, S. (1998). Plasma entry from the flanks of the near-Earth magnetotail: Geotail observations. *Journal of Geophysical Research*, *103*(A3), 4391–4408. https://doi.org/10.1029/97JA03340

Fuselier, S. A., Dayeh, M. A., Livadiotis, G., McComas, D. J., Ogasawara, K., Valek, P., et al. (2015). Imaging the development of the cold dense plasma sheet, Geophys. *Res. Lett.*, *42*(19), 7867–7873. https://doi.org/10.1002/2015GL065716

Fuselier, S. A., Trattner, K. J., & Petrinec, S. M. (2011). Antiparallel and component reconnection at the dayside magnetopause. *Journal of Geophysical Research*, *116*(A10), A10227. https://doi.org/10.1029/2011JA016888

Gonzalez, W. D., Joselyn, J. A., Kamide, Y., Kroehl, H. W., Rostoker, G., Tsurutani, B. T., & Vasyliunas, V. M. (1994). What is a geomagnetic storm? *Journal of Geophysical Research*, *99*(A4), 5771–5792. https://doi.org/10.1029/93JA02867

Gordeev, E., Sergeev, V., Merkin, V., & Kuznetsova, M. (2017). On the origin of plasma sheet reconfiguration during the substorm growth phase. *Geophysical Research Letters*, *44*(17), 8696–8702. https://doi.org/10.1002/2017GL074539

Guzdar, P. N., Shao, X., Goodrich, C. C., Papadopoulos, K., Wiltberger, M. J., & Lyon, J. G. (2001). Three-dimensional MHD simulations of the steady state magnetosphere with northward interplanetary magnetic field. *Journal of Geophysical Research*, *106*(A1), 275–287. https://doi.org/10.1029/2000JA000066

Hasegawa, H., Fujimoto, M., Phan, T. D., Rème, H., Balogh, A., Dunlop, M. W., et al. (2004). Transport of solar wind into Earth's magnetosphere through rolled-up Kelvin–Helmholtz vortices. *Nature*, *430*(7001), 755–758. https://doi.org/10.1038/nature02799

Henderson, M. G. (2004). The May 2–3, 1986 CDAW-9C interval: A sawtooth event. *Geophysical Research Letters*, *31*(11), L11804. https://doi.org/10.1029/2004GL019941

Hill, T. W., & Reiff, P. H. (1980). Plasma-sheet dynamics and magnetospheric substorms. *Planetary and Space Science*, *28*(4), 363–374. https://doi.org/10.1016/0032-0633(80)90040-9

Hu, Y. Q., Peng, Z., Wang, C., & Kan, J. R. (2009). Magnetic merging line and reconnection voltage versus IMF clock angle: Results from global MHD simulations. *Journal of Geophysical Research*, *114*(A8), A08220. https://doi.org/10.1029/2009JA014118

Huang, C. S., Reeves, G. D., Borovsky, J. E., Skoug, R. M., Pu, Z. Y., & Le, G. (2003). magnetospheric substorms and their relationship with solar wind variations. *Journal of Geophysical Research*, *108*(A6), 1255. https://doi.org/10.1029/2002JA009704

Johnson, J. R., & Wing, S. (2009). Northward interplanetary magnetic field plasma sheet entropies. *Journal of Geophysical Research*, *114*(A9), A00D08. https://doi.org/10.1029/2008JA014017

Kan, J. R., & Lee, L. C. (1979). Energy coupling function and solar wind-magnetosphere dynamo. *Geophysical Research Letters*, *6*(7), 577–580. https://doi.org/10.1029/GL006i007p00577

Kessel, R. L., Chen, S., Green, J. L., Fung, S. F., Boardsen, S. A., Tan, L. C., et al. (1996). Evidence of high latitude reconnecting during northward IMF: Hawkeye observations. *Geophysical Research Letters*, *23*(5), 583–586. https://doi.org/10.1029/95gl03083

Kistler, L. M., Asamura, K., Kasahara, S., Miyoshi, Y., Mouikis, C. G., Keika, K., et al. (2023). The variable source of the plasma sheet during a geomagnetic storm. *Nature Communications*, *14*(1), 6143. https://doi.org/10.1038/s41467-023-41735-3

Lane, J. H., Grocott, A., & Case, N. A. (2022). The influence of localized dynamics on dusk-dawn convection in the Earth's magnetotail. *Journal of Geophysical Research: Space Physics*, *127*(5), e2021JA030057. https://doi.org/10.1029/2021JA030057

Lazzeri, C., Samsonov, A., Forsyth, C., Branduardi-Raymont, G., & Bogdanova, Y. V. (2024). A statistical study of the properties of, and geomagnetic responses to, large, rapid southward turnings of the interplanetary magnetic field. *Journal of Geophysical Research: Space Physics*, *129*(9), e2023JA032160. https://doi.org/10.1029/2023JA032160

Li, W., Raeder, J., Dorelli, J., Øieroset, M., & Phan, T. D. (2005). Plasma sheet formation during long period of northward IMF. *Geophysical Research Letters*, *32*(12), L12S08. https://doi.org/10.1029/2004GL021524

Li, W., Raeder, J., Thomsen, M. F., & Lavraud, B. (2008). Solar wind plasma entry into the magnetosphere under northward IMF conditions. *Journal of Geophysical Research*, *113*(A4), A04204. https://doi.org/10.1029/2007JA012604

Li, W., Wu, L., Ge, Y., & Lü, L. Z. (2021). Magnetotail configuration under northward IMF conditions. *Journal of Geophysical Research: Space Physics*, *126*(2), e2020JA028634. https://doi.org/10.1029/2020JA028634

Lindqvist, P. A., Olsson, G., Torbert, R. B., King, B., Granoff, M., Rau, D., et al. (2016). The spin-plane double probe electric field instrument for MMS. *Space Science Reviews*, *199*(1–4), 137–165. https://doi.org/10.1007/s11214-014-0116-9

Ma, X., Nykyri, K., Dimmock, A., & Chu, C. (2020). Statistical study of solar wind, magnetosheath, and magnetotail plasma and field properties: 12+ years of THEMIS observations and MHD simulations. *Journal of Geophysical Research: Space Physics*, *125*(10), e2020JA028209. https://doi.org/10.1029/2020JA028209

Maezawa, K., Hori, T., Mukai, T., Saito, Y., Yamamoto, T., Kokubun, S., & Nishida, A. (1997). Structure of the distant magnetotail and its dependence on the IMF by component: GEOTAIL observations. *Advances in Space Research*, *20*(4–5), 949–959. https://doi.org/10.1016/s0273-1177(97)00503-6

McPherron, Hsu, T., & Chu, X. (2015). An optimum solar wind coupling function for the AL index. *Journal of Geophysical Research: Space Physics*, *120*(4), 2494–2515. https://doi.org/10.1002/2014JA020619

McPherron, R. L. (1970). Growth phase of magnetospheric substorms. *Journal of Geophysical Research*, *75*(28), 5592–5599. https://doi.org/10.1029/JA075i028p05592

Miura, A. (1984). Anomalous transport by magnetohydrodynamic Kelvin-Helmholtz instabilities in the solar wind-magnetosphere interaction. *Journal of Geophysical Research*, *89*(A2), 801–818. https://doi.org/10.1029/JA089iA02p00801

Myllys, M., Kilpua, E., & Pulkkinen, T. (2015). Solar-wind control of plasma sheet dynamics. *Annales Geophysicae*, *33*(7), 845–855. https://doi.org/10.5194/angeo-33-845-2015

Newell, P. T., & Liou, K. (2011). Solar wind driving and substorm triggering. *Journal of Geophysical Research*, *116*(A3), A03229. https://doi.org/10.1029/2010JA016139

Newell, P. T., Sibeck, D. G., & Meng, C.-I. (1995). Penetration of the interplanetary magnetic field, by and magnetosheath plasma into the magnetosphere: Implications for the predominant magnetopause merging site. *Journal of Geophysical Research*, *100*(A1), 235–243. https://doi.org/10.1029/94JA02632

Nishimura, Y., Kikuchi, T., Wygant, J., Shinbori, A., Ono, T., Matsuoka, A., et al. (2009). Response of convection electric fields in the magnetosphere to IMF orientation change. *Journal of Geophysical Research*, *114*(A9), A09206. https://doi.org/10.1029/2009JA014277

Ogino, T., Walker, R. J., & Ashour-Abdalla, M. (1994). A global magnetohydrodynamic simulation of the response of the magnetosphere to a northward turning of the interplanetary magnetic field. *Journal of Geophysical Research*, *99*(A6), 11027–11042. https://doi.org/10.1029/93JA03313

Ohma, A., Østgaard, N., Laundal, K. M., Reistad, J. P., Hatch, S. M., & Tenfjord, P. (2021). Evolution of IMF by induced asymmetries: The role of tail reconnection. *Journal of Geophysical Research: Space Physics*, *126*(7), e2021JA029577. https://doi.org/10.1029/2021JA029577

Øieroset, M. J., Raeder, J., Phan, T. D., Wing, S., McFadden, J. P., Li, W., et al. (2005). Global cooling and densification of the plasma sheet during an extended period of purely northward IMF on October 22-24, 2003. *Geophysical Research Letters*, *32*, L12S07. https://doi.org/10.1029/2004GL021523

Park, K. S., Lee, D.-Y., Ogino, T., & Lee, D. H. (2015). MHD simulations using average solar wind conditions for substorms observed under northward IMF conditions. *Journal of Geophysical Research: Space Physics*, *120*(9), 7672–7686. https://doi.org/10.1002/2015JA021005

Peng, Z., Wang, C., Yang, Y. F., Li, H., Hu, Y. Q., & Du, J. (2013). Substorms under northward interplanetary magnetic field: Statistical study. *Journal of Geophysical Research*, *118*(1), 364–374. https://doi.org/10.1029/2012JA018065

Petrukovich, A. A., Baumjohann, W., Nakamura, R., Balogh, A., Mukai, T., Glassmeier, K.-H., et al. (2003). Plasma sheet structure during strongly northward IMF. *Journal of Geophysical Research*, *108*(A6), 1258. https://doi.org/10.1029/2002JA009738

Phan, T. D., & Paschmann, G. (1996). Low-latitude dayside magnetopause and boundary layer for high magnetic shear: 1. Structure and motion. *Journal of Geophysical Research*, *101*(A4), 7801–7815. https://doi.org/10.1029/95JA03752

Phan, T. D., Paschmann, G., Gosling, J. T., Oieroset, M., Fujimoto, M., Drake, J. F., & Angelopoulos, V. (2013). The dependence of magnetic reconnection on plasma β and magnetic shear: Evidence from magnetopause observations. *Geophysical Research Letters*, *40*(1), 11–16. https://doi.org/10.1029/2012GL054528

Pitkänen, T., Kullen, A., & Chong, G. S. (2024). Importance of the dusk-dawn interplanetary magnetic field component (IMF By) to magnetospheric convection in Earth's magnetotail plasma sheet. *Frontiers in Astronomy and Space Sciences*, *11*, 1373249. https://doi.org/10.3389/fspas.2024.1373249

Pitkänen, T., Kullen, A., Shi, Q. Q., Hamrin, M., De Spiegeleer, A., & Nishimura, Y. (2018). Convection electric field and plasma convection in a twisted magnetotail: A THEMIS case study 1–2 January 2009. *Journal of Geophysical Research: Space Physics*, *123*(9), 7486–7497. https://doi.org/10.1029/2018JA025688

Pollock, C., Moore, T., Jacques, A., Burch, J., Gliese, U., Saito, Y., et al. (2016). Fast plasma investigation for magnetospheric multiscale. *Space Science Reviews*, *199*(1–4), 331–406. https://doi.org/10.1007/s11214-016-0245-4

Richard, R. L., Walker, R. J., & Ashour-Abdalla, M. (1994). The population of the magnetosphere by solar winds ions when the interplanetary magnetic field is northward. *Geophysical Research Letters*, *21*(23), 2455–2458. https://doi.org/10.1029/94GL01427

Rong, Z. J., Lui, A. T. Y., Wan, W. X., Yang, Y. Y., Shen, C., Petrukovich, A. A., et al. (2015). Time delay of interplanetary magnetic field penetration into Earth's magnetotail. *Journal of Geophysical Research: Space Physics*, *120*(5), 3406–3414. https://doi.org/10.1002/2014JA020452

Rostoker, G., Akasofu, S. I., Baumjohann, W., Kamide, Y., & McPherron, R. (1988). The roles of direct input of energy from the solar wind and unloading of stored magnetotail energy in driving magnetospheric substorms. *Space Science Reviews*, *46*(1–2), 93–111. https://doi.org/10.1007/BF00173876

Runov, A., Angelopoulos, V., Artemyev, A. V., Weygand, J. M., Lu, S., Lin, Y., & Zhang, X.-J. (2021). Global and local processes of thin current sheet formation during substorm growth phase. *Journal of Atmospheric and Solar-Terrestrial Physics*, *220*, 105671. https://doi.org/10.1016/j.jastp.2021

Russell, C. T., Anderson, B. J., Baumjohann, W., Bromund, K. R., Dearborn, D., Fischer, D., et al. (2016). The magnetospheric multiscale magnetometers. *Space Science Reviews*, *199*(1–4), 189–256. https://doi.org/10.1007/s11214-014-0057-3

Samsonov, A., Milan, S., Buzulukova, N., Sibeck, D., Forsyth, C., Branduardi-Raymont, G., & Dai, L. (2024). Time sequence of magnetospheric responses to a southward IMF turning. *Journal of Geophysical Research: Space Physics*, *129*(7), e2023JA032378. https://doi.org/10.1029/2023JA032378

Schödel, R., Nakamura, R., Baumjohann, W., & Mukai, T. (2001). Rapid flux transport and plasma sheet reconfiguration. *Journal of Geophysical Research*, *106*(A5), 8381–8390. https://doi.org/10.1029/2000JA900159

Snekvik, K., Østgaard, N., Tenfjord, P., Reistad, J. P., Laundal, K. M., Milan, S. E., & Haaland, S. E. (2017). Dayside and nightside magnetic field responses at 780 km altitude to dayside reconnection. *Journal of Geophysical Research: Space Physics*, *122*(2), 1670–1689. https://doi.org/10.1002/2016JA023177

Song, P., DeZeeuw, D. L., Gombosi, T. I., Groth, C. P. T., & Powell, K. G. (1999). A numerical study of solar wind—magnetosphere interaction for northward interplanetary magnetic field. *Journal of Geophysical Research*, *104*(A12), 28361–28378. https://doi.org/10.1029/1999JA900378

21699402, 2026, 5, Downloaded from https://agupubs.onlinelibrary.wiley.com/doi/10.1029/2025JA034883 by Hui Li - Center For Space Science And Applied Research, CAS , Wiley Online Library on [21/05/2026]. See the Terms and Conditions (https://onlinelibrary.wiley.com/terms-and-conditions) on Wiley Online Library for rules of use; OA articles are governed by the applicable Creative Commons License

Southwood, D. J. (2021). A brief history of the magnetosphere. *Geophysical Monograph Series*, 1–13. https://doi.org/10.1002/9781119815624.ch1

Taguchi, S. (1992). By-controlled field-aligned currents near midnight auroral oval during northward interplanetary magnetic field. *Journal of Geophysical Research*, *97*(A8), 12231–12243. https://doi.org/10.1029/92JA00548

Tenfjord, P., Østgaard, N., Haaland, S., Snekvik, K., Laundal, K. M., Reistad, J. P., et al. (2018). How the IMF by induces a local by component during northward IMF Bz and characteristic timescales. *Journal of Geophysical Research: Space Physics*, *123*(5), 3333–3348. https://doi.org/10.1002/2018JA025186

Tenfjord, P., Østgaard, N., Snekvik, K., Laundal, K. M., Reistad, J. P., Haaland, S., & Milan, S. E. (2015). How the IMF by induces a by component in the closed magnetosphere and how it leads to asymmetric currents and convection patterns in the two hemispheres. *Journal of Geophysical Research: Space Physics*, *120*(11), 9368–9384. https://doi.org/10.1002/2015ja021579

Terasawa, T., Fujimoto, M., Mukai, T., Shinohara, I., Saito, Y., Yamamoto, T., et al. (1997). Solar wind control of density and temperature in the near-Earth plasma sheet: WIND/GEOTAIL collaboration. *Geophysical Research Letters*, *24*(8), 935–938. https://doi.org/10.1029/96gl04018

Tulasi Ram, S., Veenadhari, B., Dimri, A. P., Bulusu, J., Bagiya, M., Gurubaran, S., et al. (2024). Super-intense geomagnetic storm on 10–11 May 2024: Possible mechanisms and impacts. *Space Weather*, *22*(12), e2024SW004126. https://doi.org/10.1029/2024SW004126

Vo, T., Ergun, R. E., Usanova, M. E., & Chasapis, A. (2023). Mesoscale structure and properties of the terrestrial magnetotail plasma sheet from the Magnetospheric Multiscale mission. *Journal of Geophysical Research: Space Physics*, *128*(9), e2023JA031358. https://doi.org/10.1029/2023JA031358

Wang, C., Han, J. P., Li, H., Peng, Z., & Richardson, J. D. (2014). Solar wind–magnetosphere energy coupling function fitting: Results from a global MHD simulation. *Journal of Geophysical Research: Space Physics*, *119*(8), 6199–6212. https://doi.org/10.1002/2014JA019834

Wang, C.-P., Lyons, L. R., Nagai, T., Weygand, J. M., & McEntire, R. W. (2007). Sources, transport, and distributions of plasma sheet ions and electrons and dependences on interplanetary parameters under northward interplanetary magnetic field. *Journal of Geophysical Research*, *112*(A10), A10224. https://doi.org/10.1029/2007JA012522

Wang, J., Liu, X., Dai, F., Jiang, W., Wang, Y., Liu, A., et al. (2025). Velocity and magnetic fluctuations across machine learning defined regions of the magnetotail plasma sheet. *Journal of Geophysical Research: Space Physics*, *130*(8), e2025JA034259. https://doi.org/10.1029/2025JA034259

Wang, J., Liu, X., Dai, F., Zheng, R., Han, Y., Wang, Y., et al. (2025a). Automated plasma Region classification and boundary layer identification using machine learning. *Remote Sensing*, *17*(9), 1565. https://doi.org/10.3390/rs17091565

Wang, J. Y., Wang, C., Huang, Z. H., & Sun, T. R. (2014). Effects of the interplanetary magnetic field on the twisting of the magnetotail: Global MHD results. *Journal of Geophysical Research: Space Physics*, *119*(3), 1887–1897. https://doi.org/10.1002/2013JA019257

Wing, S., Johnson, J. R., Newell, P. T., & Meng, C.-I. (2005). Dawn-dusk asymmetries, ion spectra, and sources in the northward interplanetary magnetic field plasma sheet. *Journal of Geophysical Research*, *110*(A8), A08205. https://doi.org/10.1029/2005JA011086

Zhang, L. Q., Dai, L., Baumjohann, W., Lui, A. T. Y., Wang, C., Rème, H., & Dunlop, M. W. (2016). Temporal evolutions of the solar wind condition at 1 AU prior to the near-earth X-lines in the tail: Superposed epoch analysis. *Journal of Geophysical Research*, *121*. https://doi.org/10.1029/2016JA022687

Zhang, L. Q., Wang, C., Dai, L., Baumjohann, W., Lui, A. T. Y., Burch, J. L., et al. (2022). Vorticity within bursty bulk flows: Convective versus kinetic. *Journal of Geophysical Research: Space Physics*, *127*(3), e2020JA028934. https://doi.org/10.1029/2020JA028934

Zhang, L. Q., Wang, C., Dai, L., Ren, Y., & Lui, A. T. (2022). A statistical study on wide-amplitude kinetic Alfvénic pulse at 8–12RE in the magnetotail by THEMIS spacecraft from 2008 to 2010. *Journal of Geophysical Research: Space Physics*, *127*(2), e2021JA029593. https://doi.org/10.1029/2021JA029593

Zhang, L. Q., Wang, C., Wang, J. Y., & Lui, A. T. Y. (2019). Statistical properties of the IMF clock angle in the solar wind with northward and southward interplanetary magnetic field based on ACE observation from 1998 to 2009: Dependence on the temporal scale of the solar wind. *Advances in Space Research*. https://doi.org/10.1016/ja.asr.2018,14.094

Zhang, L. Q., Wang, J. Y., Baumjohann, W., Rème, H., Dai, L., Dunlop, M. W., et al. (2015). X-lines in the magnetotail for southward and northward IMF conditions. *Journal of Geophysical Research: Space Physics*, *120*(9), 7764–7773. https://doi.org/10.1002/2015JA021503

Zhang, L. Q., Wang, J. Y., Baumjohann, W., Rème, H., & Dunlop, M. W. (2015). Earthward and tailward flows in the plasma sheet. *Journal of Geophysical Research: Space Physics*, *120*(6), 4487–4495. https://doi.org/10.1002/2015JA021154

21699402, 2026, 5, Downloaded from https://agupubs.onlinelibrary.wiley.com/doi/10.1029/2025JA034883 by Hui Li - Center For Space Science And Applied Research, CAS , Wiley Online Library on [21/05/2026]. See the Terms and Conditions (https://onlinelibrary.wiley.com/terms-and-conditions) on Wiley Online Library for rules of use; OA articles are governed by the applicable Creative Commons License